Oxyfluoride superlattices $KTaO_3/KMF_3$ (M=Zn, Ni): Structural and electronic phenomena

A. C. Garcia-Castro,[1,2,*] Philippe Ghosez,[2] Eric Bousquet,[2] and Aldo H. Romero[3,4,†]

[1]*School of Physics, Universidad Industrial de Santander, Carrera 27 Calle 09, 680002 Bucaramanga, Colombia*

[2]*Theoretical Materials Physics, University of Liège, B-4000 Sart-Tilman, Belgium*

[3]*Department of Physics and Astronomy, West Virginia University, West Virginia-26506-6315, Morgantown, USA*

[4]*Facultad de Ingeniería-BUAP, Apartado Postal J-39, Puebla, Pue. 72570, México*

(Received 14 June 2020; revised 23 September 2020; accepted 3 December 2020; published 17 December 2020)

The structural and electronic properties of $KTaO_3/KZnF_3$ and $KTaO_3/KNiF_3$ oxyfluoride superlattices are studied from first-principles density functional theory calculations. We highlight, that beyond a critical layer thickness, these systems exhibit an insulator to metal transition that gives rise to the appearance of two-dimensional electron and hole gas, confined both, due the band alignment, within the oxide layer. The origin of the insulator to metal transition is related to the polar discontinuity at the interfaces. The behavior is discussed in terms of a simple electrostatic model and compared to that of the prototypical $LaAlO_3/SrTiO_3$ oxide system. The magnetic properties $KTaO_3/KNiF_3$ superlattices are further discussed, revealing a sizable Rashba-type spin splitting at these interfaces, much larger than in similar oxide/oxide systems.

DOI: 10.1103/PhysRevB.102.235140

I. INTRODUCTION

Unique electronic properties at oxide/oxide interfaces are accomplished by tuning the chosen constituent materials' ferroic (electric and/or magnetic) properties. This optimization is driven by the complex electron-electron interactions in strongly correlated material interfaces, which gives rise to a broad set of intriguing phenomena [1,2]. In oxide/oxide interfaces, these phenomena include the appearance of two-dimensional electron gases (2DEG) and its counterpart, two-dimensional hole gases (2DHG) at the oxide insulator/insulator interfaces [3,4], exotic electronic states due to strong spin-orbit coupling with an intriguing spin texture [5], metal-insulator transitions tunable by electric fields [6], interfacial magnetic phases [7], improper ferroelectricity [8–10], and multiferroic interactions [11]. While studies of these phenomena have focused only on complex oxide materials, there are strong indications that complex fluorides may have similar properties concerning the oxide materials.

To date, little experimental and theoretical work has been devoted to fluorides, either in bulk [12–15] or in thin-films forms [16,17], and therefore, there is minimal knowledge about their surfaces and interfacial properties [17]. In addition to the different bulk fluoride studies, much less is known about the multifunctional properties of interfaces and surfaces of complex fluorides [17]. By searching in the literature, it can be found that there are just a few reported examples of complex fluorides thin films and the corresponding interface characterization. These include $Fe/KFeF_3$ bilayers [16] and the trilayered system $Fe/KNiF_3/FeF_2$ [18] that has a dynamic and rotatable exchange anisotropy. For example, it has been reported the phenomena of exchange bias in these systems. This property is shown as a magnetic hysteresis loop center shift away from H = 0 T. The latter as a result of the magnetic interface interaction with the antiferromagnetic material. Additionally, it has been shown that $NaMnF_3$ epitaxial thin-films grown onto $SrTiO_3$ exhibit ferroelectric and magnetic behavior [17].

Recently, researchers have focused on the study and understanding of multi-ion systems. Here, oxygens in oxide perovskites are replaced with fluorine ions with different possible stoichiometries. Therefore, this process, also called fluorination, has been successfully applied to the epitaxial growth of $SrFeO_{3-x}F_x$ (x from 0 to 1) thin films [19] where substantial changes in the electric conductivity and transport properties have been demonstrated. These changes are mainly due to an induced change in the nominal oxidation state of the Fe cation. Then, and even more surprising, multifunctional properties such as superconductivity in $Sr_2CuO_2F_{2+\delta}$ [20], ionic conductivity at $BaFeF_xO_{3-\delta}$ [21], and robust antiferromagnetism in $Ba_{0.8}Sr_{0.2}FeF_xO_{3-\delta}$[22] can be tuned and/or modified in fluorinated oxides, also called oxyfluorides.

On the other hand, mixed $SrTiO_3$ and $KAgF_3$, AgF_2 interfaces were proposed where, superconducting behavior has been theoretically predicted [23,24]. Thus, oxyfluoride materials have been highlighted as materials with potential applications in the next-generation rechargeable batteries, with enhanced properties compared to their oxide counterparts [25]. Moreover, a geometrically driven ferroelectric instability [26] was stabilized under strain in the $NaMnF_3$ fluoride thin films epitaxially grown on $SrTiO_3$ [17,27], as commented before. Besides, multianionic materials (i.e., oxyfluorides, oxynitrides, and oxysulfides) have called much attention due to their potential applications in the design of novel materials [28–30]. Particularly, our computational work on fluoride perovskites (ABF_3) indicates that ABF_3/fluoride or ABF_3/ABO_3

*acgarcia@uis.edu.co

†aldo.romero@mail.wvu.edu

interfaces have unique advantages in terms of their magnetic, magnetotransport, and multiferroic properties [17,26,27].

Thus, the examples above are a few of the numerous attractive properties of high interest for science and technological applications shown by oxide and fluoride perovskites [31], which linked to the emerging field of multianion crystals highlights even more appealing possibilities [29,30]. Hence, the fundamental study of the ordered interface between an oxide and a fluoride is particularly engaging for the discovery of new phenomena for the improvement of the exotic oxide/oxide interface properties reported so far [32]. In such order of ideas, the theoretical exploration of the electronic states at oxide/fluoride interfaces, the possible existence of noncollinear ordering, and finally, the consequences of the dissimilar oxidation states, at the interface, in the electrostatic phenomena deserved more attention.

In this paper, we report a first-principles investigation of the perovskite $KTaO_3/KMF_3$ (M = Zn and Ni) interfaces and superlattices. After full geometric and electronic optimization, the system develops a two-dimensional electron gas (2DEG) and two-dimensional hole gas (2DHG). Also, the analysis of their properties in terms of an electrostatic model, across the oxyfluoride superlattices, is presented with the scrutiny of the magnetic structure for M = Ni. Finally, a Rashba-type spin splitting at the interface is examined and discussed. Based on our analysis, we hope to lead novel strategies for searching for new and complex perovskite-based oxyfluoride heterostructures.

II. COMPUTATIONAL DETAILS

We performed first-principles calculations within the density-functional theory (DFT) [33,34], as implemented in the Vienna *Ab initio* Simulation Package (VASP 5.3.3) [35,36]. We used projected augmented wave (PAW) method [37] to represent the valence and core electrons. The electronic configurations taken into account as valence electrons were: K ($3p^6 4s^1$, version 17Jan2003), Ta ($5p^6 5d^5 6s^2$, version 07Sep2000), Zn ($3d^{10} 4s^2$, version 06Sep2000), Ni ($3p^6 3d^8 4s^2$, version 06Sep2000), F ($2s^2 2p^5$, version 08Apr2002), and O ($2s^2 2p^4$, version 08Apr2002). The exchange correlation was represented within the generalized gradient approximation (GGA) with the PBEsol flavor [38]. This exchange-correlation functional has proven to be one of the most accurate XC functionals for treating oxyfluoride compounds [39]. The magnetic character was included by performing spin-polarized calculations, and the d electrons were corrected employing the DFT+U method within the Liechtenstein formalism [40] for all the $KTaO_3/KNiF_3$ superlattices. In this case, the U value was obtained by fitting the the magnetic moment per atom and the magnetic ordering obtained from DFT+U with those obtained from the HSE06 hybrid functionals [41,42] in the 1/1 superlattice. In the $KTaO_3/KZnF_3$ superlattices, no U value was included and only the DFT approach was considered. The periodic solution of these crystalline structures was represented by using Bloch states with a Γ-centered k-point mesh of $6 \times 6 \times x$ (x is selected based on the c parameter of the supercell with values of x = 4, 2, and 1 for superlattices 2/2, 4/4, and larger than 6/6, respectively) and 700 eV energy cutoff. This cutoff has been tested to give forces convergence to less than 0.001 eV Å^{-1}. Spin-orbit coupling, SOC, was included such that its effect on the electronic structure could be analyzed [43]. Born effective charges and phonon calculations were performed within the density functional perturbation theory (DFPT) [44] as implemented in the VASP code and analyzed through the Phonopy interface [45].

TABLE I. Lattice parameters, a_o, and band-gap energies, E_g, for bulk compounds. E_g values were extracted within the DFT aproach for $KTaO_3$ and $KZnF_3$, whereas the DFT+U (U = 6.0 eV) scheme was employed for $KNiF_3$. Finally, The band-gap values were also obtained by means of HSE06-based calculation [41,42].

	a_0 [Å]		E_g [eV]		
Compound	Expt.	Present	Expt.	Present	HSE06
$KTaO_3$	3.989 [56]	3.997	3.64 [56]	2.06	3.79
$KZnF_3$	4.055 [57]	4.022	–	3.90	6.31
$KNiF_3$	4.012 [57]	4.002	–	4.04	5.40

To perform calculations based on hybrid functionals for large supercells (above 2/2 ratio), and to correlate the results of the electronic structure with the DFT+U results obtained with the VASP code, we have used the linear combination of atomic orbitals (LCAO) based CRYSTAL code [46]. This code uses a Gaussian-type basis set to expand the Kohn-Sham orbitals, including polarization effects, with the advantage of a smaller basis set is required. Additionally, all the electrons were included in K, Ni, Zn, O, and F, while a pseudopotential was used for the Ta case. For the exchange-correlations term, the hybrid functionals taken into account are the B1WC [47], B3LYP [48,49], and PBEsol0 (derived from the PBE0 functional and based on the PBEsol approximation) [50] all of them with a 16%, 20%, and 25% of exact exchange-correlation term, respectively. The latter in order to investigate the correlation and functionals' effect on the calculations.

Finally, the effect of the electric field into the structure, and specifically, the piezoelectric response into the $KTaO_3$ was tested according to the implementation function-response DFPT [51–53] using the ABINIT package [54,55] and the PAW PBEsol [38] pseudopotentials and a plane wave basis expanded up to 25 Ha (680 eV). We sampled the Brillouin zone with a k-point density equivalent to a $8 \times 8 \times 8$ grid in the cubic $Pm\bar{3}m$ $KTaO_3$ under the superlattices xy strain.

III. RESULTS AND DISCUSSION

In what follows, we discuss the appearance of 2DEG and 2DHG at the $KTaO_3/KMF_3$ (M = Zn and Ni) oxyfluorides interfaces, the magnetic structure when M = Ni and finally, the Rashba spin splitting at the interface.

A. 2DEG and 2DHG

At the bulk level, $KTaO_3$ (KTO), $KZnF_3$ (KZF), and $KNiF_3$ (KNF) share the same cubic perovskite atomic structure of $Pm\bar{3}m$ symmetry, and they are all good insulators [57–60]. The theoretical and experimental data, related to the lattices parameter and band-gap energy are presented in Table I.

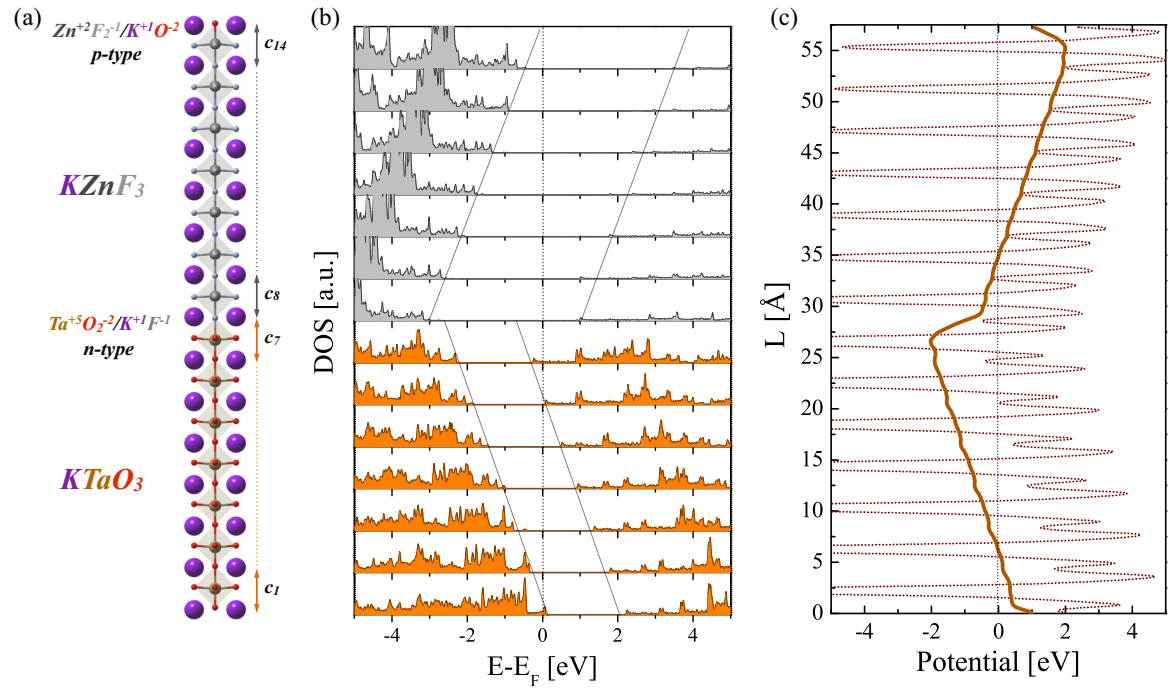

FIG. 1. (a) Sketch of the $(KTaO_3)_7/(KZnF_3)_7$ superlattice with TaO_2/KF and ZnF_2/KO interfaces and evolution of the relaxed lattice constant (K-K distance) along the stack. (b) Layer-by-layer projected electronic density of states (DOS) highlighting the presence of a 2DEG and a 2DHG at the TaO_2/KF and ZnF_2/KO interfaces, within the KTO layer. (c) Macroscopic average of the electrostatic potential along the stacking direction showing a zigzag profile confirming the presence of the electric field.

We build here stoichiometric $(KTaO_3)_n/(KMF_3)_n$ superlattices, with distinct ZnF_2/KO and TaO_2/KF (001) interfaces and in which the thickness n of each compound (in unit cells, u.c.) is ranging from 1 u.c. to 8 u.c. In each case, the in-plane lattice parameter of the superlattice is moreover set to the average of the bulk lattice constants of the two related materials (i.e., 4.022 Å for KTO/KZF and 4.001 Å for KTO/KNF). Such a choice imposes a compressive strain of -0.81% (-0.27%) on KZF (KNF) and a tensile strain of $+0.84\%$ ($+0.30\%$) on KTO in KTO/KZF (KTO/KNF) superlattices. Then, an optimization process is performed were the electronic structure, internal coordinates, and volume are allowed to relax.

Interestingly, while alternating $K^{+1}F^{-1}$ and $M^{+2}F_2^{-1}$ atomic planes are formally neutral in KZF and KNF, the $K^{+1}O^{-2}$ and $Ta^{+5}O_2^{-2}$ planes carry formal charges of -1 and $+1$ in KTO. This charge distribution means that (001)-oriented KTO/K*M*F interfaces are polar in the same way as the accessible $SrTiO_3/LaAlO_3$ interface [61]. Electric fields will, therefore, naturally develop in KTO/K*M*F superlattices, eventually giving rise to an insulator to metal transition (IMT) [62]. It is worth noticing that in such transition, an in-plane conduction and out-of plane insulator behavior is observed. Since KTO and K*M*F layers have nearly the same thickness, these fields have to be almost equal and opposite.

In Fig. 1, we report a sketch of a KTO/KZF superlattice with $n = 7$ u.c. [Fig. 1(a)]. We have included the evolution of the relaxed lattice constant along with the stack, measured from consecutive K-K distances. At the interfaces, we observe substantial atomic relaxations due to the asymmetric O-Ta-F and F-Zn-O bondings. At the same time, the lattice constant quickly converges to a homogeneous value in the interior of each layer. The lattice constant in the KZF layer (4.110 Å) is larger than the bulk value (4.055 Å), which could be explained by the compressive epitaxial strain imposed in the superlattice. However, the KTO layer similarly shows a value (4.060 Å) larger than the bulk one (3.989 Å), although it experiences a tensile epitaxial strain. This strain is compatible with the presence of electric fields within the layers and the related electrostrictive effect [63].

In Figs. 1(b) and 1(c), we report the layer-by-layer projected electronic density of states (pDOS) and the macroscopic average of the electrostatic potential along the stacking direction. As anticipated from the polar discontinuity at the interface, the electrostatic potential confirms the presence of opposite macroscopic electric fields in the two layers. This field's appearance means a polarizing electric field in KZF and a depolarizing electric field (i.e., as opposed to the formal polarization) in KTO. The pDOS also clarify the band alignment at the KTO/KZF interfaces: the band offsets are very similar at both interfaces with the valence band of KTO located $\approx$0.5 eV above the valence band of KZF and the conduction band of KTO located $\approx$1.5 eV below that of KZF. This offsetting means that both valence and conduction states in the superlattice are located in KTO. They relate respectively to O-2p and Ta-5d_{xy} states. The electric fields then produce bending of the bands. For sufficiently large thicknesses n, a Zener breakdown will appear: electrons will be transferred from the TaO_2/KF interface to the ZnF_2/KO interface giving rise to a two-dimensional hole gas (2DHG) at the first interface and a two-dimensional electron gas at the other. Due to the band alignment, this is expected to appear when the drop of potential across the KTO layer reaches the band gap of KTO, and both 2DEG and 2DHG will be located within

the KTO layer (i.e., the fluoroperovskite film will act as a condensing layer maintaining the two gases in the oxide). This boundary effect means that the situation will remain almost identical in KTO/KNF superlattices.

We see in Fig. 1(b) that the $n = 7$ KTO/KZF superlattice is metallic, with 2DEG and 2DHG indeed located in the KTO layer. Shorter superlattices (like $n = 5$, not shown here) are, however, insulating. In those cases, the opposite electric fields on both layers are equal to $\mathcal{E} \approx 100$ mV Å^{-1} (see discussion at the end of this section). Since the theoretical band gap of KTO is about 2 eV, its lattice constant is 3.997 Å and valence, and conduction states come mainly from TaO_2 planes, a Zener breakdown should appear when the distance between TaO_2 planes at both interfaces reaches five u.c., corresponding in practice to a superlattice with $n = 6$. We observe indeed that superlattices with $n \geqslant 6$ are metallic. However, we notice that the theoretical band gap of KTO is underestimated with respect to the experimental band gap of 3.64 eV [56] (3.8 eV with HSE hybrid functional). From that, we anticipate that the experimental Zener breakdown should better appear at $n \approx 10$.

At the metallic interface, we observe that the effective masses in both M = Zn and Ni cases are close to $0.3m_e$ in plane for the electrons at the 2DEG in the lowest $5d_{xy}$:Ta band. In contrast, heavier hole carriers with m^* of $1.1m_e$ are found to be localized at the $2p$-O at the KO layer. Hence, in the 2DEG at the oxyfluoride superlattices, we have at our level of approximation highly mobile carriers lighter than those reported in $SrTiO_3/LaAlO_3$ [64,65].

We notice that the electric fields within the superlattice are much larger than those previously reported for LaO/STO superlattices (58 mV Å^{-1}) [64]. In an attempt to clarify this issue, we develop an electrostatic model equivalent to the charged plates approach of Ref. [63,64]. First, the total polarization P_i in each layer i (with $i = 1$ for KTO and 2 for KZF) can be written as the sum of the polarization in zero field, P_i^0, and the polarization induced by the field $P_i^{\text{ind}} = \epsilon_0 \chi_i \mathcal{E}_i$ such that at linear order in the field:

$$P_i = P_i^0 + \epsilon_0 \chi_i \mathcal{E}_i. \tag{1}$$

Here, ϵ_0 is the vacuum dielectric permittivity while χ_i, and $\mathcal{E}_i$ are the dielectric susceptibility and electric field in each layer. Considering now, on the one hand, short-circuit boundary conditions with similar band offsets at both interfaces (i.e., $L_1\mathcal{E}_1 = -L_2\mathcal{E}_2$, where L_1 and L_2 are the KTO and KZF thicknesses) and, on the other hand, the continuity of the displacement field in the direction perpendicular to the interface (i.e., $\epsilon_0\mathcal{E}_1 + P_1 = \epsilon_0\mathcal{E}_2 + P_2$) we can deduce:

$$\mathcal{E}_1 = -\frac{L_2\left(P_1^0 - P_2^0\right)}{\epsilon_0(\epsilon_1 L_2 + \epsilon_2 L_1)}, \tag{2}$$

$$\mathcal{E}_2 = +\frac{L_1\left(P_1^0 - P_2^0\right)}{\epsilon_0(\epsilon_1 L_2 + \epsilon_2 L_1)}, \tag{3}$$

with ϵ_1 and ϵ_2 the dielectric constants of KTO and KZF. Assuming further that $L_1 = L_2$ (e.g., for $n = 7$: $L_1 = 28.49$ Å $\approx$ $L_2 = 28.69$ Å), we get finally the much simpler expression:

$$\mathcal{E}_1 = -\mathcal{E}_2 = -\frac{\left(P_1^0 - P_2^0\right)}{\epsilon_0(\epsilon_1 + \epsilon_2)}. \tag{4}$$

The fields are independent of the KTO and KMF layer thicknesses as soon as they are kept equal.

On the one hand, KZF has no formal polarization (neutral planes) and is robustly paraelectric. Even under a small compressive strain within the superlattice, it stays in a paraelectric $P4/mmm$ phase with $P_2 = 0$ and $\epsilon_2 = 9.41$ (computed in the bulk strained phase). On the other hand, KTO has a formal polarization ($e/2{\cdot}\Theta$, where Θ is the unit-cell area) related to its polar planes. This polarization can potentially develop a further spontaneous polarization P_1^s under external constraints such as an epitaxial strain or a macroscopic electric field, so that $P_1 = e/2 \cdot \Theta + P_1^s$.

If we first assume that KTO layer of the superlattice remains in a centrosymmetric $P4/mmm$ strained phase, then $P_1^s = 0$ and we compute (in bulk) $\epsilon_1 = 93.66$. Using Eq. (4) we get $\mathcal{E}_1 \approx -\mathcal{E}_2 = -54.29$ mV Å^{-1}, which is much smaller than the observed first-principles value ≈ -100 mV Å^{-1} (which suggests an effective $\epsilon_1 \approx 45$).

The epitaxially strained $P4/mmm$ phase of KTO shows an in-plane polar instability, yielding potentially the system to a $Amm2$ phase with in-plane polarization. In such case, along the z axis, $P_s^1 = 0$ again but the dielectric constant along z now becomes equal to $\epsilon_1 = 128.34$. With these values, we obtained a still smaller value $\mathcal{E}_1 \approx \mathcal{E}_2 = 40.62$ mV Å^{-1}. Moreover, in such a phase, the out-of-plane lattice constant is smaller than the in-plane one and also than the cubic one, which is in contradiction with what is observed in Fig. 2.

The c lattice parameter in the central part of the KTO layer is larger than the cubic one, and this could be explained by the presence of the strong macroscopic electric field. To check that, in Fig. 2(a) we report the change of c is a function of the applied electric field in the same direction of bulk KTO. The electric field is applied by keeping the xy-plane lattice parameters constant to the superlattice value and allowing only the z axis and internal coordinates to relax. At a field of 100 mV Å^{-1}, we observe an expansion of c of ≈0.25%. This expansion is qualitatively consistent with the expansion observed in the superlattice due to the internal electric field along the z axis. In Fig. 2(b), we then report the change of frequencies of the lowest polar mode of KTO along with different polarization directions (ω_i, with i indicating the polarization direction) when keeping the in-plane lattice constant of the superlattice, but expanding the c-lattice parameter. At the relaxed strain value measured concerning the cubic structure, only ω_{xy} mode is unstable in line with a $Amm2$ ground state. However, when the c-lattice parameter expands, ω_z is destabilized and becomes quickly much more unstable than ω_{xy}. At $c = 4.06$ Å as observed in the superlattice, ω_z is strongly unstable yielding a $P4mm$ ground state with out-of-plane polarization. All this suggests that, through the electrostrictive effect, the built-in electric field in the KTO layer might bring the system to a polar $P4mm$ state. Such a field-induced transition from para- to ferroelectric phase is similar to what can be typically observed in the paraelectric regime of regular ferroelectric like $BaTiO_3$, close above the Curie temperature [66].

In such a polar strained $P4mm$ phase with $a = b = 4.022$ Å and $c = 4.060$ Å, the bulk spontaneous polarization is $P_0^s = -27.57\ \mu\text{C cm}^{-2}$ (in line with the atomic distortion observed in the KTO layer in Fig. 1) and $\epsilon_1 = 44.65$ (the effective

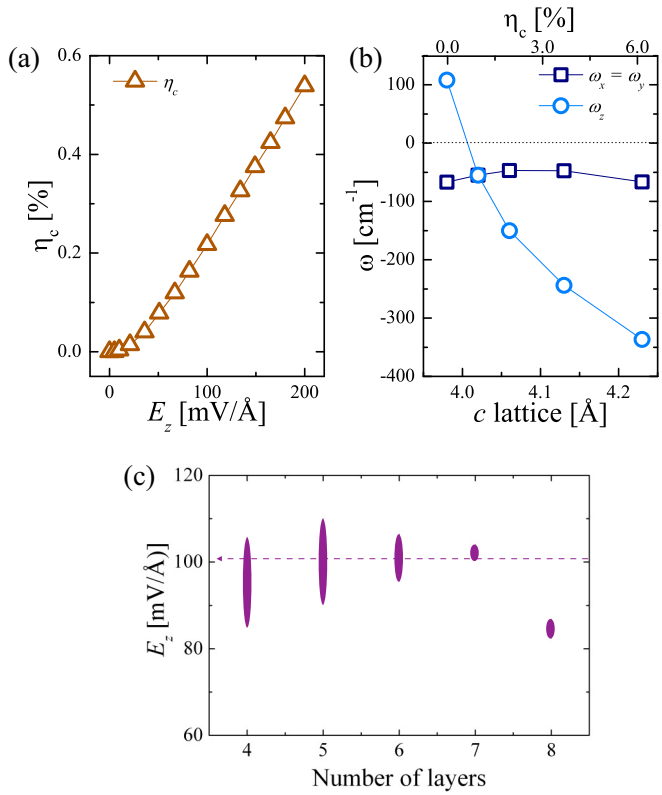

FIG. 2. (a) Electric field induced elongation, η_z, along the z axis at the $KTaO_3$. (b) Lowest polar modes at Γ point along distinct polarization directions ($\omega_x = \omega_y$, and ω_z) in the $KTaO_3$ as a function of the c-lattice elongation. Negative values correspond to imaginary frequencies. (c) Averaged electric field computed for each of the superlattices going from $n = l = 4$–8. The vertical size of the point correspond to the computed error in each case.

dielectric constant we anticipated above assuming KTO remains $P4/mmm$). Coming back to the electrostatic model and using Eq. (4), we get, however, again $\mathcal{E}_1 \approx \mathcal{E}_2 = 45.86$ mV Å^{-1}. Although, the smaller dielectric constant of this phase should *a priori* yield a larger $\mathcal{E}$, its spontaneous polarization partly screens the formal polarization [64,67], yielding again a field smaller than that observed in the superlattice.

All this suggests that KTO is less polarizable than expected from the bulk dielectric constant. Assuming that KTO is in such a $P4mm$ polar phase, the electric field of 100 mV Å^{-1} can only be explained by an effective dielectric constant $\epsilon_1 \approx 15$. This value could eventually be explained, assuming that the seven u.c. layers are made of a central five u.c. part with $\epsilon_{bulk} = 44.65$ in series with less polarizable interface 1 u.c. parts on both sides with $\epsilon_{int} = 5$. The presence of such dielectric dead layer at the interface would, however, become predominant at low thickness, suggesting that the field should increase in the insulating regime.

In Fig. 2(c), we so report the evolution of the amplitude of electric fields, equal and opposite in each layer, as a function of the layer thickness. A first observation is that the fields remain constant until $n = 7$ and then drop at $n = 8$ while the IMT appears already at $n = 6$. *A priori*, charge transfer, and field reduction, should appear from the IMT threshold. This anomaly can be traced back to the electronic band structure in Fig. 1(b): the DOS is very small in the lowest part of the conduction bands of KTO, so that a substantial transfer of charge (and drop of the field) only appear from a thickness where the Fermi level reaches the first substantial peak, which happens from $n = 8$. A second observation is that the fields seem to remain almost constant (within the accuracy of the estimate, see Fig. 1S in the Supplemental Material [68]) in the insulating regime, which is not directly supporting the existence of a low-polarizable interface layer. In such a case, the field should indeed progressively increase as the thickness decreases from 100 mV Å^{-1} for $n = 7$ to 150 mV Å^{-1} for $n = 3$ (see Fig. 2S and Table IS in the Supplemental Material [68]). However, this assumes that the frozen-in P_s and dielectric constants of the interface and middle layers are independent of thickness, which might not necessarily be the case.

In summary, KTO/KZF superlattices with polar interfaces show a behavior qualitatively similar to LAO/STO superlattices, although with slightly distinct features such as the effective mass and localization of the carriers at the interface or the critical thickness. The behavior is globally compatible with a simple electrostatic model (appearance of fields, Zener breakdown), but, contrary to LAO/STO, a quantitative agreement cannot be achieved when fitting such a model from bulk dielectric constants. Our investigations suggest that KTO might exhibit a field-induced ferroelectric transition under the electrostatic conditions of the polar interface. The system might also eventually present a dead dielectric layer at the interface. However, this cannot be fully validated from the DFT results and call for further investigations.

The same amplitude of electric field ($\mathcal{E} \approx 100$ mV Å^{-1} in the insulating regime) and behavior is observed for KTO/KNF superlattices where Ni replaces zn. Here, M = Ni induces a magnetic ordering in the system due to its magnetically active $3d$ orbital, as we discuss in the following section.

B. Magnetic ordering

We also analyzed the magnetic behavior of the oxyfluoride interfaces when M = Ni. In bulk, $KNiF_3$ shows a G-type AFM ordering with a Néel temperature of 275 K [59]. Similarly, as it was done in the M = Zn case, we studied the superlattice thickness from 2/2 to 8/8 u.c (see Fig. 3S in the Supplemental Material [68].

Initially, several magnetic orderings were tested, G-AFM, C-AFM, A-AFM, FM, and mixed G-AFM+FM layer (the FM configuration at the NiF_2 immediately after the TaO_2/KF interface and at the NiF_2/KO layers). According to our calculations, based on hybrid functionals performed with the CRYSTAL code, the ground-state magnetic ordering is always G-type AFM in the $KNiF_3$ film. These results are in full agreement with those obtained within the GGA+U approximation for U values above 6.0 eV with the VASP code. However, it is essential to mention that the mixed G-AFM+FM-layer state, (with the FM layer close to the NiF_2/KO interface), is very close in energy to the G-AFM ground state with ΔE = 0.73 meV/atom. The G-AFM+FM magnetic state is even closer than other magnetic states such as the A-AFM and C-AFM. All the energy values are shown in Table IIS in the Supplemental Material [68].

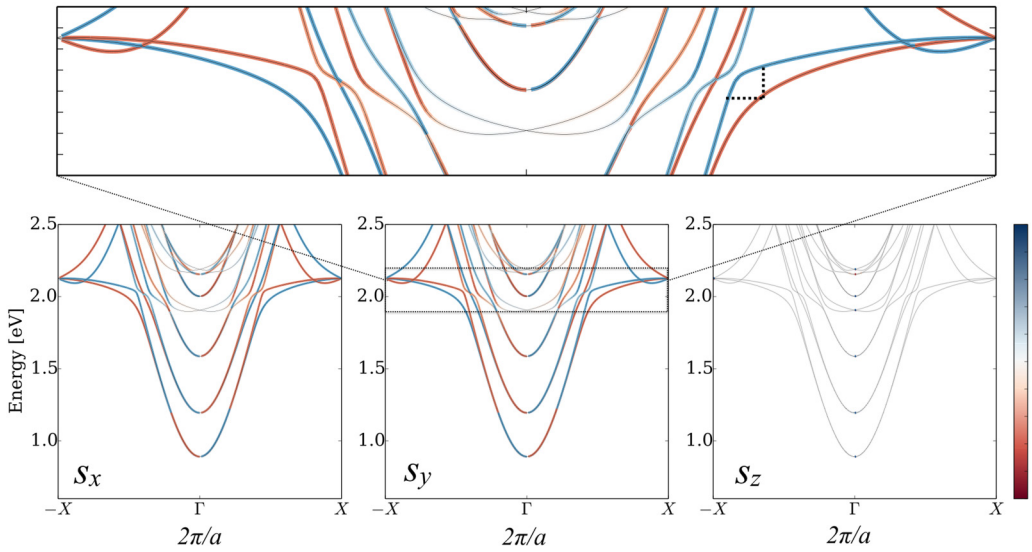

FIG. 3. Band structure for the k_x path in which, s_x, s_y, and s_z spin components are considered. The up and down orientations of the spin are represented by red and blue colors, respectively. Figure obtained with the open-source code PYPROCAR [79].

Moreover, we also found a weak magnetic moment of $m = 0.012\ \mu_B$ atom^{-1} localized on the Ta cations. These moments are following a FM interaction along z axis concerning the Ni sites ($m = 1.764\ \mu_B$ atom^{-1}) in agreement with a Ni^{+2} oxidation state. The latter is explained by the strongest FM interaction between half-occupied $3d$-Ni:e_g and the empty $5d$–Ta:t_{2g} [69] rather than an AFM interaction driven by the superexchange interaction between the Ni-O-Ta or Ta-F-Ni bonding.

Interestingly enough, there is a magnetic-moment modulation across the entire thickness of the heterostructure's magnetic slab in all the calculated superlattices (see Fig. 4S in the Supplemental Material [68]. The magnetic moment is increased at one side of the interface and decreased at the other side with tendency to reach constant value in the layer center. The 7/7 case shows a different behavior at the second side with an increase of the magnetic moment before the decrease of it. This modulation can be associated with the effect of the electric field in the Ni's oxidation state and the magnetic moment per atom, as observed previously in the $SrTiO_3/La_{0.7}Sr_{03}MnO_3$ thin films [70].

C. Cubic-Rashba spin splitting

Recently, the appearance of spin splitting followed by a complex spin texture related to a Rashba effect [71] was reported to be attained at oxide interfaces such as $SrTiO_3/LaAlO_3$ [5,72–74]. Moreover, some reports have shown similar behavior in $SrTiO_3$- and $KTaO_3$-based transistors [75,76]. In these single perovskite-based devices, a predominant k-cubic dependence of the splitting was observed in comparison to the linear term [see Eq. (5)]. The latter in agreement with the linear plus cubic dependence of the normal Rashba splitting occurring at $LaAlO_3/SrTiO_3$ interface, and mainly due to the d_{xy}-$d_{xz/yz}$ multiorbital nature of the lowest bands [73]. Additionally, in the case of Au(111) metal surface, it has been shown that even when the surface states exhibit mainly p-orbital character, the d orbitals drive the Rashba splitting and dictates the direction of the spin through the orbital-angular momentum (OAM) [77,78].

In order to look for the spin-texture and spin-orbit coupling (SOC) effects in the oxyfluoride interfaces, the analysis of the electronic structure has been performed by taking into account the SOC. Due to the high computational cost, the study of the bands was performed up to the 4/4 superlattice. For such, the electronic structure was calculated within the VASP code and analyzed within the PYPROCAR package [79]. These results can be traced up to the 7/7 system where the 2DEG and 2DHG are formed, and the IMT takes place, as shown previously. Thus, the results presented here can be extrapolated to larger n/l superlattices.

In Fig. 3 we can observe the electronic band structure along the k_x path where the s_x, s_y, and s_z spin components are presented separately and a color notation for the majority (red) and minority (blue) spin orientation is adopted. First, it is noted that the electronic structure and the spin texture at the conduction bands above of the Fermi level (and thus, close to the TaO_2/KF interface of the 7/7) are entirely 2D spin polarized in the k_x-k_y plane. Therefore, no band dispersion is observed for the s_z spin component. Surprisingly, a large spin splitting of the bands is present at the energy around 2.0 eV with respect to the Fermi energy. Additionally, the SOC effect is observed at the heavy $d_{xz/yz}$ crossing with the d_{xy} lighter bands (see the upper inset in Fig. 3).

The observed Rashba splitting is of the cubic-type character as observed in oxide surfaces, and interfaces, and it is expressed by the Hamiltonian presented in Eq. (5):

$$H_{R3} = \alpha_3 \mathcal{E}_z i(k_-^3 \sigma_+ - k_+^3 \sigma_-), \tag{5}$$

where α_3 is the cubic-Rashba coupling term, which measures the strength of the splitting (in units of eV Å^3), $\sigma_\pm = 1/2(\sigma_x \pm i\sigma_y)$ and $\sigma_{x,y}$ are the Pauli matrices. The $\mathcal{E}_z$ is the electric field perpendicular to the electron's plane movement denoted by $k_\pm = (k_x \pm ik_y)$ [75]. Here, the E vs. k profile for

the bands is represented by the relationship:

$$E^{\pm}(k) = \frac{\hbar^2 k^2}{2m^*} \pm \alpha_3 k^3. \quad (6)$$

This type of spin splitting can be understood like an opposite rotation of the lowest spin–up band with respect of the spin down around an axis fixed at the vertices of the parabolic d bands. This is in contrast with the linear horizontal displacement (or offset) of the spin–up and spin-down bands, respectively, observed in the most common linear-Rashba effect[1] present in materials such as BiTeI [80].

To obtain an idea of the order of magnitude of the spin splitting, we compare it with other perovskite-based systems. At the energy value of 2.0 eV we found that $\Delta k = 0.044$ Å^{-1}, which is more than twice of the one found at the $KTaO_3$-based transistor (i.e., Au/parylene-Al/$KTaO_3$) [81]. Besides, the energy difference between up- and down- spins is $\Delta E = 64$ meV at the same bands, as shown in Fig. 3. To compare with oxide/oxide interface, we computed the spin-texture of the $SrTiO_3/LaAlO_3$ system under the same conditions in a 4/4 superlattice (not shown here). We found that $\Delta k = 0.011$ Å^{-1} and a $\Delta E = 11$ meV. Then, this spin splitting is four times smaller in comparison to 0.044 Å^{-1} and 64 meV at the oxyfluoride interface.

It is important to note that the SOC in the Ta is at least 11 times larger than the one in the Ti cation. This energy splitting can be taken as an advantage in the mixed oxide/fluoride interfaces. This difference can be due to the significant disparity in lattice parameters of the fluoride perovskites. This difference will allow the incorporation of a more prominent perovskite oxide with $4d$ and $5d$ orbitals. This mismatch provides for new design rules for superlattices and interfaces with mixed properties.

From the magnetic $KTaO_3/KNiF_3$ superlattice, we noticed that the same spin texture remains at the TaO_2/KO. Nonetheless, the spin texture is becoming more complicated due to the overlapping of the $5d$:Ta band with the unoccupied $3d(e_g)$:Ni states above the Fermi level. It is essential to take advantage of the fact that the magnetic properties can be conserved in $KNiF_3$. Then, mixed multifunctional properties of 2DEG+2DHG+k^3-Rashba-splitting+G-AFM could be condensed in the same heterostructure. Therefore, other possible properties can be engineered in these heterostructures, which is worth to be investigated in future works.

Moreover, it is worth noticing that the relevance of the k^3-Rashba dependence has been highlighted in the field of multifunctional properties based on the significant difference in the effective field symmetry between the k linear and the k^3 Rashba. Thus, the k^3 symmetry influences all of the SOC related phenomena in materials, which is not the case of the k-linear Rashba term. For example, in the case of the spin Hall effect, it has been predicted that the k-cubic Rashba term can give rise to a more significant spin Hall conductivity [82,83].

Remarkably, as the polarization and the magnetic ordering close to the interface increases, a more complex behavior of the spin texture could be expected. Therefore, further studies focused on the exploration of the spin texture in the fluoride/oxide interfaces, by using complementary theoretical approaches as proposed in Refs. [84,85], could provide additional insights on the physics behind spin transport at the interfaces.

Finally, in this system, the possible tuning of the energy position of the $5d$:Ta bands concerning the Fermi energy, by controlling the n/l ratio, stand as an additional feature of these systems. Therefore, the amount of splitting and, consequently, the spin-transport properties can be tuned as well, which makes this type of interface even more appealing. Moreover, in the $M =$ Ni superlattices case, the transport at the interface could be affected by the magnetization giving, as a result, a Hall conductivity that worth to be explored in further analysis.

IV. CONCLUSIONS

We have studied the electronic and structural properties of oxyfluorides $(KTaO_3)_n/(KMF_3)_l$ $M =$ Zn and Ni interfaces from first-principles calculations. We found that an IMT occurs in these superlattices, due to the polar discontinuity at the interfaces. The IMT appears for a critical layer thickness n larger than in LAO/STO superlattices despite the large electric fields in the two layers. Due to the band alignment, both resulting 2DEG and 2DHG are confined within the oxide layer, and the 2DEG show particularly low effective masses. Fitting the DFT data with an electrostatic model with bulk parameters does not provide a quantitative agreement; it suggests that KTO might experience a field-induced ferroelectric transition in the built-in field and, the possible presence of a dead dielectric layer at the interface, although this should be further studied.

We also observed that the magnetism in the $KTaO_3/KNiF_3$ exhibits a moment magnitude modulation but keeping on average the bulk G-type AFM. Surprisingly, we observed a large k^3-Rashba-type splitting at the oxyfluoride interfaces, at least four times larger than the one reported in $SrTiO_3/LaAlO_3$ interface and twice that of the $KTaO_3$-based transistor. Thus, we believe that the oxyfluoride superlattices can be highlighted as novel perovskite-based systems where rich multifunctional properties can be tuned as in their oxides/oxides counterparts.

ACKNOWLEDGMENTS

This work used XSEDE facilities, which are supported by the National Science Foundation under Grant No. ACI-1053575. The authors also acknowledge the support from the Texas Advances Computer Center (with the Stampede2 and Bridges supercomputers), the PRACE project TheDeNoMo and on the CECI facilities funded by F.R.S-FNRS (Grant No. 2.5020.1) and Tier-1 supercomputer of the Fédération Wallonie-Bruxelles funded by the Walloon Region (Grant No. 1117545). This work was supported by the DMREF-NSF 1434897, NSF OAC-1740111 and DOE DE-SC0016176 projects. We acknowledge the West Virginia University supercomputing clusters; Spruce Knob and Thorny Flat which were used for the development of the library. E.B. acknowledge the support from the FNRS (project MULAN No. J.0020.20). A.C.G.C. acknowledge the support from the GridUIS-2

[1]The linear-Rashba effect has the E vs. k form: $E^{\pm}(k) = (\hbar^2 k^2/2m^*) \pm \alpha|k|$ coming from the Hamiltonian of the form $H_R = \alpha \mathcal{E}_z i(k_- \sigma_+ - k_+ \sigma_-)$.

experimental testbed, developed under the Universidad Industrial de Santander (SC3-UIS) High Performance and Scientific Computing Centre, with support from UIS Vicerrectoria de Investigación y Extensión (VIE-UIS) and several UIS research groups as well as other funding resources. A.C.G.C. also acknowledge the support from the Vicerrectoría de Investigación y Extensión (with its 2019 - Call) that allowed E.B. to visit the Universidad Industrial de Santander.

[1] H. Y. Hwang, Y. Iwasa, M. Kawasaki, B. Keimer, N. Nagaosa, and Y. Tokura, Emergent phenomena at oxide interfaces, Nature Mater. **11**, 103 (2012).

[2] F. Granozio, G. Koster, and G. Rijnders, Functional oxide interfaces, MRS Bull. **38**, 1017 (2013).

[3] J. Mannhart, D. Blank, H. Hwang, A. Millis, and J.-M. Triscone, Two-dimensional electron gases at oxide interfaces, MRS Bull. **33**, 1027 (2008).

[4] A. Joshua, S. Pecker, J. Ruhman, E. Altman, and S. Ilani, A universal critical density underlying the physics of electrons at the LaAlO(3)/SrTiO(3) interface., Nature Commun. **3**, 1129 (2012).

[5] S. Caprara, F. Peronaci, and M. Grilli, Intrinsic Instability of Electronic Interfaces with Strong Rashba Coupling, Phys. Rev. Lett. **109**, 196401 (2012).

[6] P. Zubko, S. Gariglio, M. Gabay, P. Ghosez, and J.-M. Triscone, Interface physics in complex oxide heterostructures, Annu. Rev. Condens. Matter Phys. **2**, 141 (2011).

[7] B. R. K. Nanda and S. Satpathy, Polar catastrophe, electron leakage, and magnetic ordering at the $LaMnO_3/SrMnO_3$ interface, Phys. Rev. B **81**, 224408 (2010).

[8] E. Bousquet, M. Dawber, N. Stucki, C. Lichtensteiger, P. Hermet, S. Gariglio, J.-M. Triscone, and P. Ghosez, Improper ferroelectricity in perovskite oxide artificial superlattices., Nature (London) **452**, 732 (2008).

[9] N. A. Benedek and C. J. Fennie, Hybrid Improper Ferroelectricity: A Mechanism for Controllable Polarization-Magnetization Coupling, Phys. Rev. Lett. **106**, 107204 (2011).

[10] A. T. Mulder, N. A. Benedek, J. M. Rondinelli, and C. J. Fennie, Turning ABO_3 antiferroelectrics into ferroelectrics: Design rules for practical rotation-driven ferroelectricity in double perovskites and $A_3B_2O_7$ ruddlesden-popper compounds, Adv. Funct. Mater. **23**, 4810 (2013).

[11] Z. Zanolli, J. C. Wojdeł, J. Íñiguez, and P. Ghosez, Electric control of the magnetization in $BiFeO_3/LaFeO_3$ superlattices, Phys. Rev. B **88**, 060102(R) (2013).

[12] M. A. Carpenter, E. K. H. Salje, and C. J. Howard, Magnetoelastic coupling and multiferroic ferroelastic/magnetic phase transitions in the perovskite $kmnf_3$, Phys. Rev. B **85**, 224430 (2012).

[13] D. P. Dobson, S. A. Hunt, A. Lindsay-Scott, and I. G. Wood, Towards better analogues for $MgSiO_3$ post-perovskite: $NaCoF_3$ and $NaNiF_3$, two new recoverable fluoride post-perovskites, Phys. Earth Planet. Inter. **189**, 171 (2011).

[14] P. J. Edwardson, L. L. Boyer, R. L. Newman, D. H. Fox, J. R. Hardy, J. W. Flocken, R. A. Guenther, and W. Mei, Ferroelectricity in perovskitelike $NaCaF_3$ predicted *ab initio*, Phys. Rev. B **39**, 9738 (1989).

[15] C.-g. Duan, W. N. Mei, J. Liu, W.-G. Yin, J. R. Hardy, R. W. Smith, M. J. Mehl, and L. L. Boyer, Electronic properties of $nacdf_3$: A first-principles prediction, Phys. Rev. B **69**, 033102 (2004).

[16] W. Pang, R. L. Stamps, L. Malkinski, Z. Celinski, and D. Skrzypek, Exchange bias system of $Fe/KFeF_3$, J. Appl. Phys. **95**, 7309 (2004).

[17] M. Yang, A. KC, A. C. Garcia-Castro, P. Borisov, E. Bousquet, D. Lederman, A. H. Romero, and C. Cen, Room temperature ferroelectricity in fluoroperovskite thin films, Sci. Rep. **7**, 7182 (2017).

[18] S. Widuch, R. L. Stamps, D. Skrzypek, and Z. Celinski, Dynamic and rotatable exchange anisotropy in $Fe/KNiF_3$ /FeF_2 trilayers, J. Phys. D **44**, 415003 (2011).

[19] E. J. Moon, Y. Xie, E. D. Laird, D. J. Keavney, C. Y. Li, and S. J. May, Fluorination of epitaxial oxides: Synthesis of perovskite oxyfluoride thin films, J. Am. Chem. Soc. **136**, 2224 (2014).

[20] M. AI-Mamouri, P. P. Edwards, C. Greaves, and M. Slaski, Synthesis and superconducting properties of the strontium copper oxy-fluoride $Sr_2CuO_2F_{2+\delta}$, Nature (London) **369**, 382 (1994).

[21] M. Sturza, S. Daviero-Minaud, H. Kabbour, O. Gardoll, and O. Mentre, Fluorination of iron hexagonal perovskites promoting low temperature oxygen mobility, Chem. Mater. **22**, 6726 (2010).

[22] M. Sturza, H. Kabbour, S. Daviero-Minaud, D. Filimonov, K. Pokholok, N. Tiercelin, F. Porcher, L. Aldon, and O. Mentre, Unprecedented robust antiferromagnetism in fluorinated hexagonal perovskites, J. Am. Chem. Soc. **133**, 10901 (2011).

[23] X. Yang and H. Su, Cuprate-like electronic properties in superlattices with Ag(II)F? square sheet., Sci. Rep. **4**, 5420 (2014).

[24] X. Yang and H. Su, Electronic Properties of Fluoride and Half?fluoride Superlattices $KZnF_3/KAgF_3$ and $SrTiO_3/KAgF_3$, Sci. Rep. **5**, 15849 (2015).

[25] D. Deng, Transition metal oxyfluorides for next-generation rechargeable batteries, ChemNanoMat **3**, 146 (2017).

[26] A. C. Garcia-Castro, N. A. Spaldin, A. H. Romero, and E. Bousquet, Geometric ferroelectricity in fluoroperovskites, Phys. Rev. B **89**, 104107 (2014).

[27] A. C. Garcia-Castro, A. H. Romero, and E. Bousquet, Strain-engineered multiferroicity in *Pnma*$NaMnF_3$ fluoroperovskite, Phys. Rev. Lett. **116**, 117202 (2016).

[28] N. Charles, R. J. Saballos, and J. M. Rondinelli, Structural Diversity from Anion Order in Heteroanionic Materials, Chem. Mater. **30**, 3528 (2018).

[29] H. Kageyama, K. Hayashi, K. Maeda, J. P. Attfield, Z. Hiroi, J. M. Rondinelli, and K. R. Poeppelmeier, Expanding frontiers in materials chemistry and physics with multiple anions, Nat. Commun. **9**, 772 (2018).

[30] J. K. Harada, N. Charles, K. R. Poeppelmeier, and J. M. Rondinelli, Heteroanionic Materials by Design: Progress Toward Targeted Properties, Adv. Mater. **31**, 1805295 (2019).

[31] A. Tressaud and K. Poeppelmeier, *Photonic and Electronic Properties of Fluoride Materials: Progress in Fluorine Science Series* (Elsevier Inc., Amsterdam, 2016).

[32] M. Dawber and E. Bousquet, New developments in artificially layered ferroelectric oxide superlattices, MRS Bull. **38**, 1048 (2013).

[33] P. Hohenberg and W. Kohn, Inhomogeneous electron gas, Phys. Rev. **136**, B864 (1964).

[34] W. Kohn and L. J. Sham, Self-consistent equations including exchange and correlation effects, Phys. Rev. **140**, A1133 (1965).

[35] G. Kresse and J. Furthmüller, Efficient iterative schemes for ab initio total-energy calculations using a plane-wave basis set., Phys. Rev. B **54**, 11169 (1996).

[36] G. Kresse and D. Joubert, From ultrasoft pseudopotentials to the projector augmented-wave method, Phys. Rev. B **59**, 1758 (1999).

[37] P. E. Blöchl, Projector augmented-wave method, Phys. Rev. B **50**, 17953 (1994).

[38] J. P. Perdew, A. Ruzsinszky, G. I. Csonka, O. A. Vydrov, G. E. Scuseria, L. A. Constantin, X. Zhou, and K. Burke, Restoring the Density-Gradient Expansion for Exchange in Solids and Surfaces, Phys. Rev. Lett. **100**, 136406 (2008).

[39] N. Charles and J. M. Rondinelli, Assessing exchange-correlation functional performance for structure and property predictions of oxyfluoride compounds from first principles, Phys. Rev. B **94**, 174108 (2016).

[40] A. I. Liechtenstein, V. I. Anisimov, and J. Zaanen, Density-functional theory and strong interactions: Orbital ordering in mott-hubbard insulators, Phys. Rev. B **52**, R5467 (1995).

[41] J. Heyd, G. E. Scuseria, and M. Ernzerhof, Hybrid functionals based on a screened coulomb potential, J. Chem. Phys. **118**, 8207 (2003).

[42] A. V. Krukau, O. A. Vydrov, A. F. Izmaylov, and G. E. Scuseria, Influence of the exchange screening parameter on the performance of screened hybrid functionals, J. Chem. Phys. **125**, 224106 (2006).

[43] D. Hobbs, G. Kresse, and J. Hafner, Fully unconstrained noncollinear magnetism within the projector augmented-wave method, Phys. Rev. B **62**, 11556 (2000).

[44] X. Gonze and C. Lee, Dynamical matrices, born effective charges, dielectric permittivity tensors, and interatomic force constants from density-functional perturbation theory, Phys. Rev. B **55**, 10355 (1997).

[45] A. Togo and I. Tanaka, First principles phonon calculations in materials science, Scr. Mater. **108**, 1 (2015).

[46] R. Dovesi, R. Orlando, B. Civalleri, C. Roetti, V. R. Saunders, and C. M. Zicovich-Wilson, CRYSTAL: A computational tool for the *ab initio* study of the electronic properties of crystals, Zeitschrift Kristallographie - Crystalline Materials **220**, 571 (2005).

[47] D. I. Bilc, R. Orlando, R. Shaltaf, G.-M. Rignanese, J. Íñiguez, and P. Ghosez, Hybrid exchange-correlation functional for accurate prediction of the electronic and structural properties of ferroelectric oxides, Phys. Rev. B **77**, 165107 (2008).

[48] A. D. Becke, A new mixing of hartree-fock and local density-functional theories, J. Chem. Phys. **98**, 1372 (1993).

[49] A. D. Becke, Density-functional thermochemistry. i. the effect of the exchange-only gradient correction, J. Chem. Phys. **96**, 2155 (1992).

[50] J. P. Perdew, M. Ernzerhof, and K. Burke, Rationale for mixing exact exchange with density functional approximations, J. Chem. Phys. **105**, 9982 (1996).

[51] M. Stengel, N. A. Spaldin, and D. Vanderbilt, Electric displacement as the fundamental variable in electronic-structure calculations, Nature Phys. **5**, 304 (2009).

[52] I. Souza, J. Íñiguez, and D. Vanderbilt, First-Principles Approach to Insulators in Finite Electric Fields, Phys. Rev. Lett. **89**, 117602 (2002).

[53] J. Hong and D. Vanderbilt, Mapping the energy surface of $pbtio_3$ in multidimensional electric-displacement space, Phys. Rev. B **84**, 115107 (2011).

[54] X. Gonze, B. Amadon, G. Antonius, F. Arnardi, L. Baguet, J.-M. Beuken, J. Bieder, F. Bottin, J. Bouchet, E. Bousquet, N. Brouwer, F. Bruneval, G. Brunin, T. Cavignac, J.-B. Charraud, W. Chen, M. Côté, S. Cottenier, J. Denier, G. Geneste, P. Ghosez, M. Giantomassi, Y. Gillet, O. Gingras, D. R. Hamann, G. Hautier, X. He, N. Helbig, N. Holzwarth, Y. Jia, F. Jollet, W. Lafargue-Dit-Hauret, K. Lejaeghere, M. A. Marques, A. Martin, C. Martins, H. P. Miranda, F. Naccarato, K. Persson, G. Petretto, V. Planes, Y. Pouillon, S. Prokhorenko, F. Ricci, G.-M. Rignanese, A. H. Romero, M. M. Schmitt, M. Torrent, M. J. van Setten, B. V. Troeye, M. J. Verstraete, G. Zérah, and J. W. Zwanziger, The ABINIT project: Impact, environment and recent developments, Comput. Phys. Commun. **248**, 107042 (2020).

[55] X. Gonze, F. Jollet, F. A. Araujo], D. Adams, B. Amadon, T. Applencourt, C. Audouze, J.-M. Beuken, J. Bieder, A. Bokhanchuk, E. Bousquet, F. Bruneval, D. Caliste, M. Côté, F. Dahm, F. D. Pieve, M. Delaveau, M. D. Gennaro, B. Dorado, and C. Espejo, Recent developments in the ABINIT software package, Comput. Phys. Commun. **205**, 106 (2016).

[56] G. E. Jellison, I. Pauluskas, L. A. Boatner, and D. J. Singh, Optical functions of $KTaO_3$ as determined by spectroscopic ellipsometry and comparison with band structure calculations, Phys. Rev. B **74**, 155130 (2006).

[57] K. Knox, Perovskite-like fluorides. I. Structures of $KMnF_3$, $KFeF_3$, $KNiF_3$ and $KZnF_3$. Crystal field effects in the series and in $KCrF_3$ and $KCuF_3$, Acta Crystallogr. **14**, 583 (1961).

[58] O. Madelung, U. Rössler, and M. Schulz, eds., $KTaO_3$ crystal structure, lattice parameters, thermal expansion, in *Ternary Compounds, Organic Semiconductors* (Springer, Berlin, 2000) pp. 1–3.

[59] A. Okazaki, Y. Suemune, and T. Fuchikami, The crystal structures of $KMnF_3$, $KFeF_3$, $KCoF_3$, $KNiF_3$ and $KCuF_3$, J. Phys. Soc. Jpn. **14**, 1823 (1959).

[60] G. Pari, S. Mathi Jaya, and R. Asokamani, Electronic structure and magnetism of KMF_3 (M = Mn,Fe,Co,Ni), Phys. Rev. B **50**, 8166 (1994).

[61] A. Ohtomo and H. Hwang, A high-mobility electron gas at the $LaAlO_3/SrTiO_3$ heterointerface, Nature (London) **427**, 423 (2004).

[62] N. C. Bristowe, P. Ghosez, P. B. Littlewood, and E. Artacho, The origin of two-dimensional electron gases at oxide interfaces: insights from theory, J. Phys.: Condens. Matter **26**, 143201 (2014).

[63] C. Cancellieri, D. Fontaine, S. Gariglio, N. Reyren, A. D. Caviglia, A. Fête, S. J. Leake, S. A. Pauli, P. R. Willmott, M. Stengel, P. Ghosez, and J.-M. Triscone, Electrostriction at the $LaAlO_3/SrTiO_3$ interface, Phys. Rev. Lett. **107**, 056102 (2011).

[64] N. C. Bristowe, E. Artacho, and P. B. Littlewood, Oxide superlattices with alternating *p* and *n* interfaces, Phys. Rev. B **80**, 045425 (2009).

[65] P. Delugas, A. Filippetti, V. Fiorentini, D. I. Bilc, D. Fontaine, and P. Ghosez, Spontaneous 2-Dimensional Carrier Confinement at the *n*-Type $SrTiO_3/LaAlO_3$ Interface, Phys. Rev. Lett. **106**, 166807 (2011).

[66] W. J. Merz, Double hysteresis loop of $batio_3$ at the curie point, Phys. Rev. **91**, 513 (1953).

[67] P. Aguado-Puente, N. C. Bristowe, B. Yin, R. Shirasawa, P. Ghosez, P. B. Littlewood, and E. Artacho, Model of two-dimensional electron gas formation at ferroelectric interfaces, Phys. Rev. B **92**, 035438 (2015).

[68] See Supplemental Material at http://link.aps.org/supplemental/10.1103/PhysRevB.102.235140 for more information on the electronic structure, electrostatic potential at different superlattices thicknesses, and magnetic analysis.

[69] P. Yu, Y. Chu, and R. Ramesh, Oxide interfaces: pathways to novel phenomena, Materials Today **15**, 320 (2012).

[70] R. Trappen, A. C. Garcia-Castro, V. T. Tra, C. Y. Huang, W. Ibarra-Hernandez, J. Fitch, S. Singh, J. Zhou, G. Cabrera, Y. H. Chu, J. M. LeBeau, A. H. Romero, and M. B. Holcomb, Electrostatic potential and valence modulation in $La_{0.7}Sr_{0.3}MnO_3$ thin films, Sci. Rep. **8**, 14313 (2018).

[71] Y. A. Bychkov and E. I. Rashba, Oscillatory effects and the magnetic susceptibility of carriers in inversion layers, J. Phys. C **17**, 6039 (1984).

[72] A. D. Caviglia, M. Gabay, S. Gariglio, N. Reyren, C. Cancellieri, and J.-M. Triscone, Tunable Rashba Spin-Orbit Interaction at Oxide Interfaces, Phys. Rev. Lett. **104**, 126803 (2010).

[73] Z. Zhong, A. Tóth, and K. Held, Theory of spin-orbit coupling at $LaAlO_3/SrTiO_3$ interfaces and $SrTiO_3$ surfaces, Phys. Rev. B **87**, 161102(R) (2013).

[74] S. Hurand, A. Jouan, C. Feuillet-Palma, G. Singh, J. Biscaras, E. Lesne, N. Reyren, A. Barthélémy, M. Bibes, J. E. Villegas, C. Ulysse, X. Lafosse, M. Pannetier-Lecoeur, S. Caprara, M. Grilli, J. Lesueur, and N. Bergeal, Field-effect control of superconductivity and rashba spin-orbit coupling in top-gated $LaAlO_3/SrTiO_3$ devices, Sci. Rep. **5**, 12751 (2015).

[75] H. Nakamura, T. Koga, and T. Kimura, Experimental Evidence of Cubic Rashba Effect in an Inversion-Symmetric Oxide, Phys. Rev. Lett. **108**, 206601 (2012).

[76] H. Nakamura and T. Kimura, Electric field tuning of spin-orbit coupling in $KTaO_3$ field-effect transistors, Phys. Rev. B **80**, 121308(R) (2009).

[77] H. Lee and H. J. Choi, Role of *d* orbitals in the rashba-type spin splitting for noble-metal surfaces, Phys. Rev. B **86**, 045437 (2012).

[78] S. R. Park and C. Kim, Microscopic mechanism for the rashba spin-band splitting: Perspective from formation of local orbital angular momentum, J. Electron Spectrosc. Relat. Phenom. **201**, 6 (2015), special issue on electron spectroscopy for Rashba spin-orbit interaction.

[79] U. Herath, P. Tavadze, X. He, E. Bousquet, S. Singh, F. Muñoz, and A. H. Romero, PyProcar: A Python library for electronic structure pre/post-processing, Computer Phys. Commun. **251**, 107080 (2020).

[80] K. Ishizaka, M. S. Bahramy, H. Murakawa, M. Sakano, T. Shimojima, T. Sonobe, K. Koizumi, S. Shin, H. Miyahara, A. Kimura, K. Miyamoto, T. Okuda, H. Namatame, M. Taniguchi, R. Arita, N. Nagaosa, K. Kobayashi, Y. Murakami, R. Kumai, Y. Kaneko, Y. Onose, and Y. Tokura, Giant Rashba-type spin splitting in bulk bitei, Nature Mater **10**, 521 (2011).

[81] P. D. C. King, R. H. He, T. Eknapakul, P. Buaphet, S.-K. Mo, Y. Kaneko, S. Harashima, Y. Hikita, M. S. Bahramy, C. Bell, Z. Hussain, Y. Tokura, Z.-X. Shen, H. Y. Hwang, F. Baumberger, and W. Meevasana, Subband Structure of a Two-Dimensional Electron Gas Formed at the Polar Surface of the Strong Spin-Orbit Perovskite $KTaO_3$, Phys. Rev. Lett. **108**, 117602 (2012).

[82] O. Bleibaum and S. Wachsmuth, Spin hall effect in semiconductor heterostructures with cubic rashba spin-orbit interaction, Phys. Rev. B **74**, 195330 (2006).

[83] R. Moriya, K. Sawano, Y. Hoshi, S. Masubuchi, Y. Shiraki, A. Wild, C. Neumann, G. Abstreiter, D. Bougeard, T. Koga, and T. Machida, Cubic Rashba Spin-Orbit Interaction of a Two-Dimensional Hole Gas in a Strained-Ge/SiGe Quantum Well, Phys. Rev. Lett. **113**, 086601 (2014).

[84] R. Ozawa, S. Hayami, and Y. Motome, Zero-Field Skyrmions with a High Topological Number in Itinerant Magnets, Phys. Rev. Lett. **118**, 147205 (2017).

[85] Z. Wang, Y. Su, S.-Z. Lin, and C. D. Batista, Skyrmion Crystal from RKKY Interaction Mediated by 2D Electron Gas, Phys. Rev. Lett. **124**, 207201 (2020).